

PAPER • OPEN ACCESS

Influence of morphology on electrical and optical properties of graphene/Al-doped ZnO-nanorod composites

To cite this article: Ebrahim Chalangar *et al* 2018 *Nanotechnology* **29** 415201

View the [article online](#) for updates and enhancements.

Related content

- [The effect of cation doping on the morphology, optical and structural properties of highly oriented wurtzite ZnO-nanorod arrays grown by a hydrothermal method](#)
A Hassanpour, P Guo, S Shen et al.
- [Effects of Aluminium Doping and Electrode Distance on the Performance of Aligned Zinc Oxide Nanorod Array-Based Ultraviolet Photoconductive Sensors](#)
Mohamad Hafiz Mamat, Zuraida Khusaimi, Musa Mohamed Zahidi et al.
- [Tunable white light from photo- and electroluminescence of ZnO nanoparticles](#)
Jorge Oliva, Leonardo Perez Mayen, Elder De la Rosa et al.





IOP | ebooks™

Bringing you innovative digital publishing with leading voices to create your essential collection of books in STEM research.

Start exploring the collection - download the first chapter of every title for free.

Influence of morphology on electrical and optical properties of graphene/Al-doped ZnO-nanorod composites

Ebrahim Chalanger^{1,2} , Houssaine Machhadani³, Seung-Hyuk Lim³,
K Fredrik Karlsson³, Omer Nur¹ , Magnus Willander¹ and
Håkan Pettersson^{1,2,4}

¹ Department of Science and Technology (ITN), Faculty of Science & Engineering, Linköping University, Norrköping, Sweden

² Department of Mathematics, Physics and Electrical Engineering, Halmstad University, Halmstad, Sweden

³ Semiconductor Materials, Department of Physics, Chemistry, and Biology (IFM), Linköping University, Linköping, Sweden

⁴ Solid State Physics and NanoLund, Lund University, Lund, Sweden

E-mail: hakan.pettersson@hh.se

Received 15 May 2018, revised 26 June 2018

Accepted for publication 17 July 2018

Published 1 August 2018



Abstract

The development of future 3D-printed electronics relies on the access to highly conductive inexpensive materials that are printable at low temperatures (<100 °C). The implementation of available materials for these applications are, however, still limited by issues related to cost and printing quality. Here, we report on the simple hydrothermal growth of novel nanocomposites that are well suited for conductive printing applications. The nanocomposites comprise highly Al-doped ZnO nanorods grown on graphene nanoplatelets (GNPs). The ZnO nanorods play the two major roles of (i) preventing GNPs from agglomerating and (ii) promoting electrical conduction paths between the graphene platelets. The effect of two different ZnO-nanorod morphologies with varying Al-doping concentration on the nanocomposite conductivity and the graphene dispersity are investigated. Time-dependent absorption, photoluminescence and photoconductivity measurements show that growth in high pH solutions promotes a better graphene dispersity, higher doping levels and enhanced bonding between the graphene and the ZnO nanorods. Growth in low pH solutions yields samples characterized by a higher conductivity and a reduced number of surface defects. These samples also exhibit a large persistent photoconductivity attributed to an effective charge separation and transfer from the nanorods to the graphene platelets. Our findings can be used to tailor the conductivity of novel printable composites, or for fabrication of large volumes of inexpensive porous conjugated graphene-semiconductor composites.

Keywords: graphene, zinc oxide, nanorods, nanocomposites, persistent photoconductivity, printing

(Some figures may appear in colour only in the online journal)

1. Introduction

The development of 3D-printing technologies for realizing electronic components and materials is evolving very quickly. Presently, there is a strong interest in developing novel 3D-printable



Original content from this work may be used under the terms of the [Creative Commons Attribution 3.0 licence](https://creativecommons.org/licenses/by/3.0/). Any further distribution of this work must maintain attribution to the author(s) and the title of the work, journal citation and DOI.

functional nanocomposites for device fabrication. For instance, conductive nanocomposites can be optimized for low-temperature printing of conductors using the well-developed fused deposition modeling printers available on the market today [1–3]. Carbon-based nanocomposite materials, containing graphene in particular, are inexpensive attractive candidates with remarkable physical properties that make them well suited for 3D-printing of electronics [4–6].

Demonstrated properties that make graphene promising for electronics include excellent (i) carrier mobility (up to $10^6 \text{ cm}^2 \text{ V}^{-1} \text{ s}^{-1}$) [7], (ii) electrical resistivity ($0.1\text{--}6 \text{ k}\Omega/\square$ for a single layer with 97.7% optical transparency) [7], (iii) chemical stability and (iv) mechanical strength (double to that of CNTs) [7]. However, graphene is highly hydrophobic and hardly interacts with other materials. Moreover, the high-aspect-ratio of graphene nanoplatelets (GNPs), combined with large van der Waals forces typically lead to issues with undesired agglomeration into large particles. In order to use graphene in printing applications, it must therefore be properly dispersed in a suitable medium. High-quality dispersions are typically facilitated by introducing chemical surfactants, [8] which unfortunately influence the electrical properties of graphene in an undesired way. A different approach to synthesize a conductive screen printing graphene ink with a resistance of $30 \Omega/\square$ at $25 \mu\text{m}$ thickness by gelation of a graphene dispersion was recently reported [9]. Despite all of these efforts it still remains a challenge to make a highly conductive graphene dispersion in a viscous medium, suitable for printing applications.

Here we propose a new approach to realize a graphene dispersion, effectively forming a conductive network, by growing zinc oxide nanorods (ZnO-NRs), degenerately doped with aluminum (Al), as highly conductive spacers on the surface of the GNPs. The potential advantages of these composites stem from the remarkable charge transport characteristics of graphene, combined with the excellent optical characteristics of ZnO. The expected enhancement of the optoelectronic properties of this composite might lead to important applications in optoelectronics, photovoltaics and photocatalysis [10].

Zinc oxide is a well-known unintentionally n-type semiconductor with a wide direct bandgap of $3.2\text{--}3.4 \text{ eV}$ at room-temperature. It can be grown in different nanostructured shapes e.g. nanorods by inexpensive low-temperature ($<100^\circ\text{C}$) hydrothermal solution-based procedures [11, 12]. The morphology, length and diameter of the ZnO-NRs can be controlled by tuning the pH value, temperature of the growth solution, precursor concentration and growth duration [13].

ZnO-NRs can be grown on GNPs with excellent result despite of their hydrophobicity. It has been shown that the reduced lattice mismatch of less than 2% [14, 15] between ZnO-NRs and GNPs causes strong atomic level interactions which lead to strong bonding and high mechanical stability [16]. Moreover, the electrical interface between GNPs and ZnO-NRs shows excellent low-ohmic metallic behavior [17, 18] of great importance for conductive applications.

2. Experimental details

All the chemicals required for the hydrothermal growth presented in this work, including the multilayer GNP powder, were purchased from Sigma-Aldrich. The first step was to seed the GNPs with a layer of ZnO nanoparticles (ZnO-NPs) [19]. GNPs with a concentration of 0.5 g l^{-1} were initially dispersed in DI-water using an ultrasonic bath for 10 min. Subsequently this solution was mixed with a 100 ml solution of 0.005 M of zinc acetate ($\text{Zn}(\text{CH}_3\text{COO})_2 \cdot 2\text{H}_2\text{O}$) and 0.025 M of KOH in water at 60°C in an ultrasonic bath for 10 min. The seeded GNPs were subsequently washed in water and centrifuged (3000 rpm, 10 min) three times, followed by annealing in nitrogen at 300°C for 30 min to enhance the attachment of the ZnO-NPs to the GNPs. For the growth of ZnO-NRs, we prepared two solutions of 0.025 M of $\text{Zn}(\text{NO}_3)_2 \cdot 6\text{H}_2\text{O}$ and 0.025 M of $\text{C}_6\text{H}_{12}\text{N}_4$ (HMT) in DI-water with pH 6.6 and pH 11 (by adding ammonia), respectively. These two different pH growth solutions resulted in significantly different ZnO-NRs morphologies. A 0.002 M aqueous solution of $\text{Al}(\text{NO}_3)_3 \cdot 9\text{H}_2\text{O}$ was stirred overnight and added to the growth solution to supply the Al for doping of the NRs. Finally the seeded GNPs were added to the growth solution under stirring for 2 h at 75°C .

3. Results and discussion

Figure 1(a) shows a schematic of the grown nanostructures. The ZnO:Al-NRs play two major roles for the final composites. First, they make a physical spacer between the GNPs proportional to their length. These physical spacers prevent GNPs from agglomerating and make the structure more porous. The porosities can, depending on the application, be filled by a proper matrix material. Second, degenerately doped ZnO-NRs grown on one GNP will form low-ohmic electrical connections to a neighboring GNP. Previous studies have shown that the formation of low-resistance direct contacts between the particles is the most crucial factor for realization of highly conductive polymer composites [20]. The sharp NRs can also more easily penetrate through any polymer matrix filling up the porosities between the GNPs and increase the probability of direct contact formation between GNPs. The overall electrical transport properties depend on the resulting complex conductive network between the GNPs in the matrix.

To make sure that the ZnO-NPs in the seed layer are also doped with Al, a piece of pure Al was inserted into the solution during the seeding of the GNPs. The high pH value of 13 of the seed solution will lead to a partially dissolving of Al in the solution and to doping of the ZnO-NPs [21]. Figure 1(b) shows GNPs decorated with ZnO:Al-NPs. The photoluminescence (PL) measurements discussed below clearly show the effects of the high Al-doping on the optical properties of the ZnO-NPs.

The two different morphologies of ZnO-NRs grown at different pH (6.6 and 11) were investigated for better performance

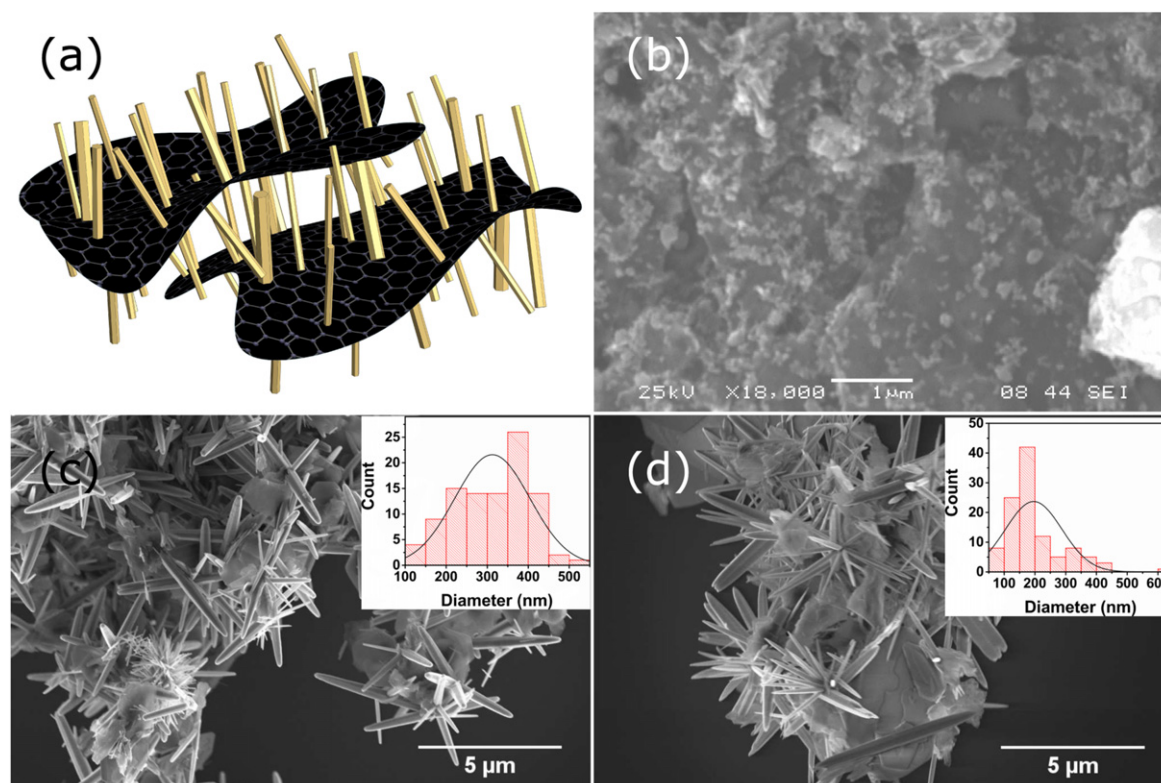


Figure 1. (a) Schematics of ZnO-NRs grown on both sides of GNPs by the hydrothermal solution-based procedure. (b) Scanning electron microscopy (SEM) image of GNPs decorated with Al-doped ZnO nanoparticles. (c) Thick hexagonal low-density ZnO-NRs grown at pH 6.6. (d) Thin needle-like, high-density ZnO-NRs grown at pH 11. The insets show the size distribution of the nanorods diameter.

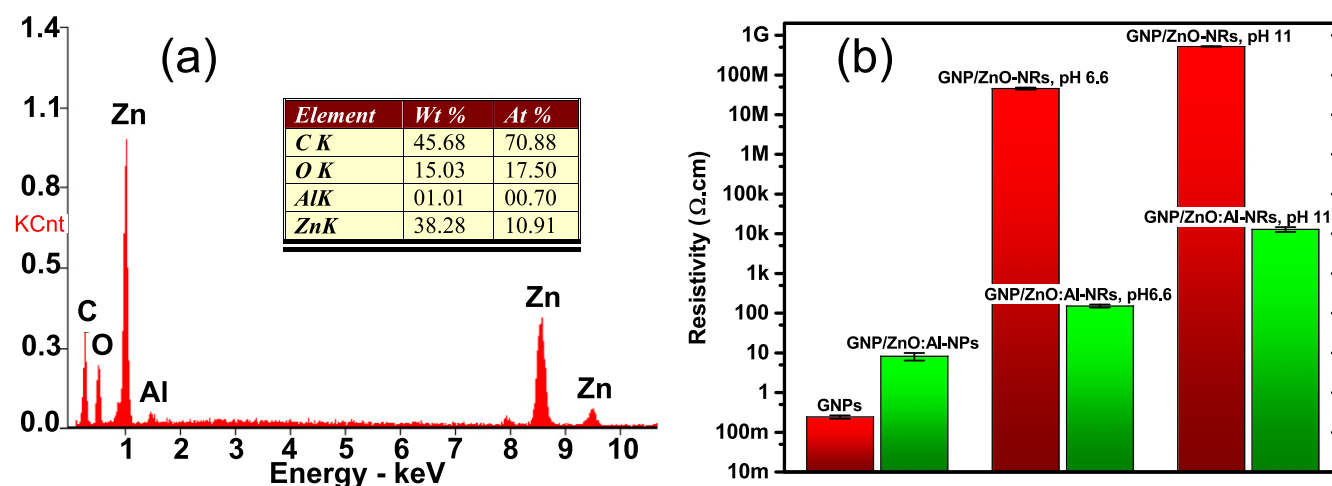


Figure 2. (a) Energy dispersive x-ray spectroscopy (EDS) spectra for GNP/ZnO:Al-NRs grown in pH 11. (b) Resistivity of GNPs, GNP/ZnO:Al-NPs, GNP/ZnO-NRs (pH 6.6 and 11) and GNP/ZnO:Al-NRs (pH 6.6 and 11) measured by a four-point probe method.

regarding both conductivity and dispersity. ZnO-NRs grown at pH 6.6 (figure 1(c)) are hexagonal, thicker (mean diameter 313 nm), longer (1–2 μm) and more sparse compared to ZnO-NRs grown at pH 11. The NRs grown at high pH are more needle-like with a mean diameter and length of 196 nm and 0.5–1.5 μm respectively (figure 1(d)). The density of ZnO-NRs on the GNP surface was estimated, $1.4 \mu\text{m}^{-2}$ for the samples grown at pH 6.6 and $2.4 \mu\text{m}^{-2}$ for the samples grown at pH 11 by counting in the SEM image.

Figure 2(a) shows the abundance of different elements in the samples extracted from energy dispersive x-ray spectroscopy (EDS). Carbon (C) is the most abundant element observed in all composites with an atomic ratio of 6.5 compared to Zn. The presence of 0.5–1.5 at% Al is also detected in the doped composites, which basically represents the lower boundary for a typical EDS system. The doping concentration in the samples is estimated in the range of 0.7–1.2 at% based on the dopant concentration in the growth solution [22, 23]. The presence of

oxygen (O) is almost 60 at% higher than Zn in the samples. This excess of O could be related to the hydroxyl groups OH^- and/or carboxyl groups $-\text{COOH}$, or to adsorbed water on the GNPs or ZnO surfaces during the synthesis [24].

The resistivity of the composite layer samples, comprising the investigated microparticles, is measured by a standard four-point method. To do that, the layered materials must first be smoothly deposited. To deposit the randomized GNP/ZnO:Al-NRs microparticles, we used a vacuum filtration method [8]. A water dispersion containing the microparticles was filtered by an Anodisc membrane filter from Whatman (25 mm diameter, $0.2\ \mu\text{m}$ poresize) and dried at 70°C in an oven. The layer thickness, varying from 20 to $50\ \mu\text{m}$, was measured by a contact profilometer. As shown in figure 2(b), the resistivity of pure GNPs is the lowest and it increases after decoration with ZnO:Al-NPs. This increase can be explained by the synthesis procedure and/or the spacing induced by the doped ZnO nanoparticles. Growth of undoped ZnO-NRs on the decorated GNPs results in a further increase of the resistivity for both investigated morphologies, effectively converting the layers to insulators. This high resistivity shows that the GNPs are physically separated from each other by the non-intentionally doped ZnO-NRs. For the doped samples, the resistivity strongly decreased and the nanocomposites again became conductive due to the enhanced conductivity of the degenerately doped ZnO:Al-NRs. This shows that the electrical current is passing through the ZnO-NRs. The ZnO-NRs (nanoneedles) grown at pH 11 show a comparably higher resistivity compared to those grown at pH 6.6. This suggests that nanoneedle-shaped GNPs are better dispersed. This hypothesis is supported by the optical UV-vis data discussed below.

To compare the dispersity of the two morphologies, and the attachment of ZnO-NRs to the GNPs, time-dependent UV-vis spectroscopy was employed. Figures 3(a)–(c) show the absorption spectra of the GNPs with different morphologies of grown ZnO:Al-NRs, dispersed in isopropanol, after every 5 min and after 24 h. The absorption spectra of pure GNPs exhibit a rather flat absorption characteristics dominated by spectral features beyond 1500 nm related to hydroxyl and/or carboxyl groups on the GNP surfaces (figure 3(a)). Figures 3(b) and (c) display a strong absorption peak at about 380 nm for dispersions of GNP/ZnO:Al-NRs due to the ZnO bandgap. The broad absorption shoulder, and spectrally unresolved absorption edge, reflect various scattering mechanisms [25] in the samples, which lead to strong spectral convolution effects. The dispersions of GNPs and GNP/ZnO:Al-NRs grown at pH 11 show a uniform decrease in absorption with excitation time due to particles settling. Figure 3(b) shows that the absorption in GNP/ZnO:Al-NRs grown at a pH 6.6 changes non-uniformly with wavelength. The long wavelength absorption response in our dispersions is dominated by the GNPs, while it relates to ZnO at short wavelength. The non-uniform decrease in absorption observed in 3(b) indicates the presence of two phases (separated GNPs and ZnO:Al-NRs) in the dispersion. The ZnO:Al-NRs settle faster than the GNPs. In contrast, GNP/ZnO:Al-NRs grown at a pH 11 forms a single phase in the dispersion, as evident from the uniform settling rate in figure 3(c). This

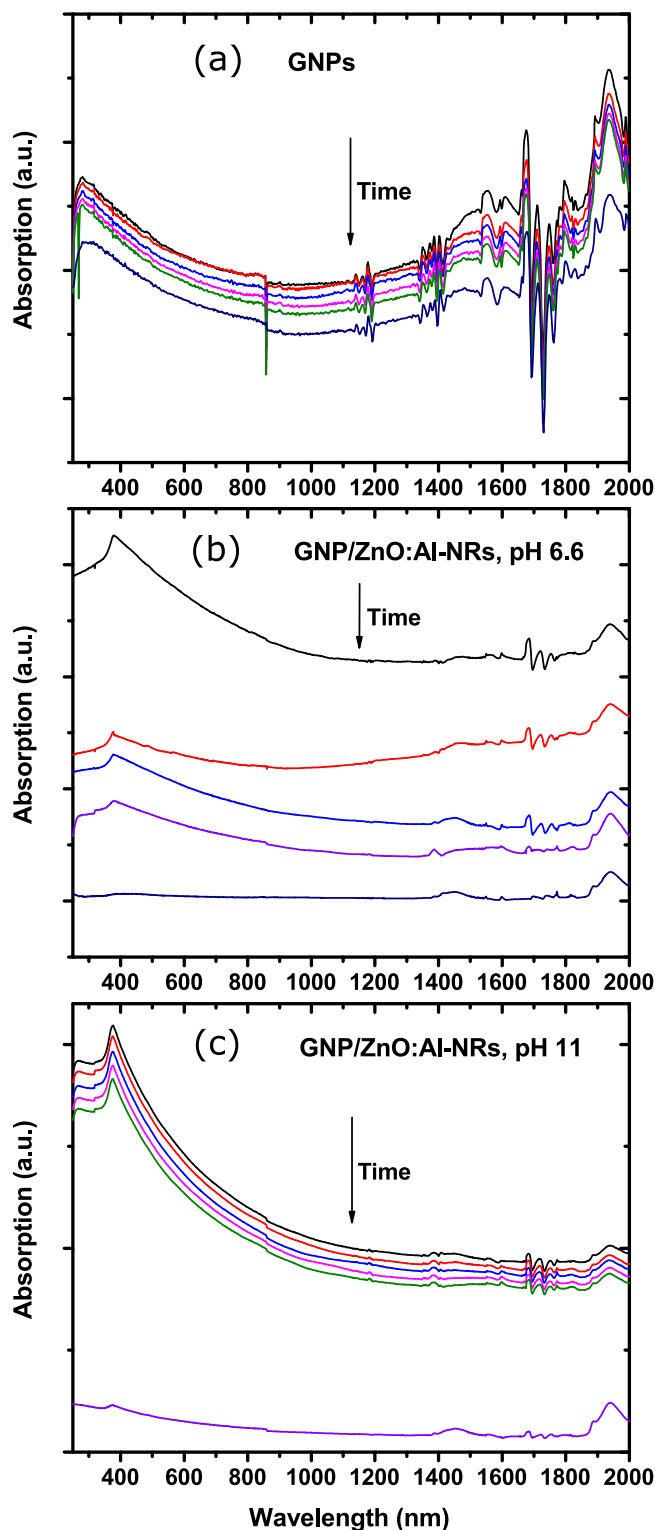


Figure 3. Time-dependent UV-vis spectroscopy. Temporal evolution of the absorption spectra after 0, 5, 10, 15, 20 min and 24 h, respectively, for the dispersion of (a) GNPs, (b) GNP/ZnO:Al-NRs grown at pH 6.6 and (c) GNP/ZnO:Al-NRs grown at pH 11 in isopropanol. (Figure (a) has a different vertical scale.)

implies that ZnO:Al-NRs are better attached to GNPs in high pH growth solutions.

To study the quality of bonding between the GNPs and the ZnO-NRs, and also to see the effects of Al-doping level in

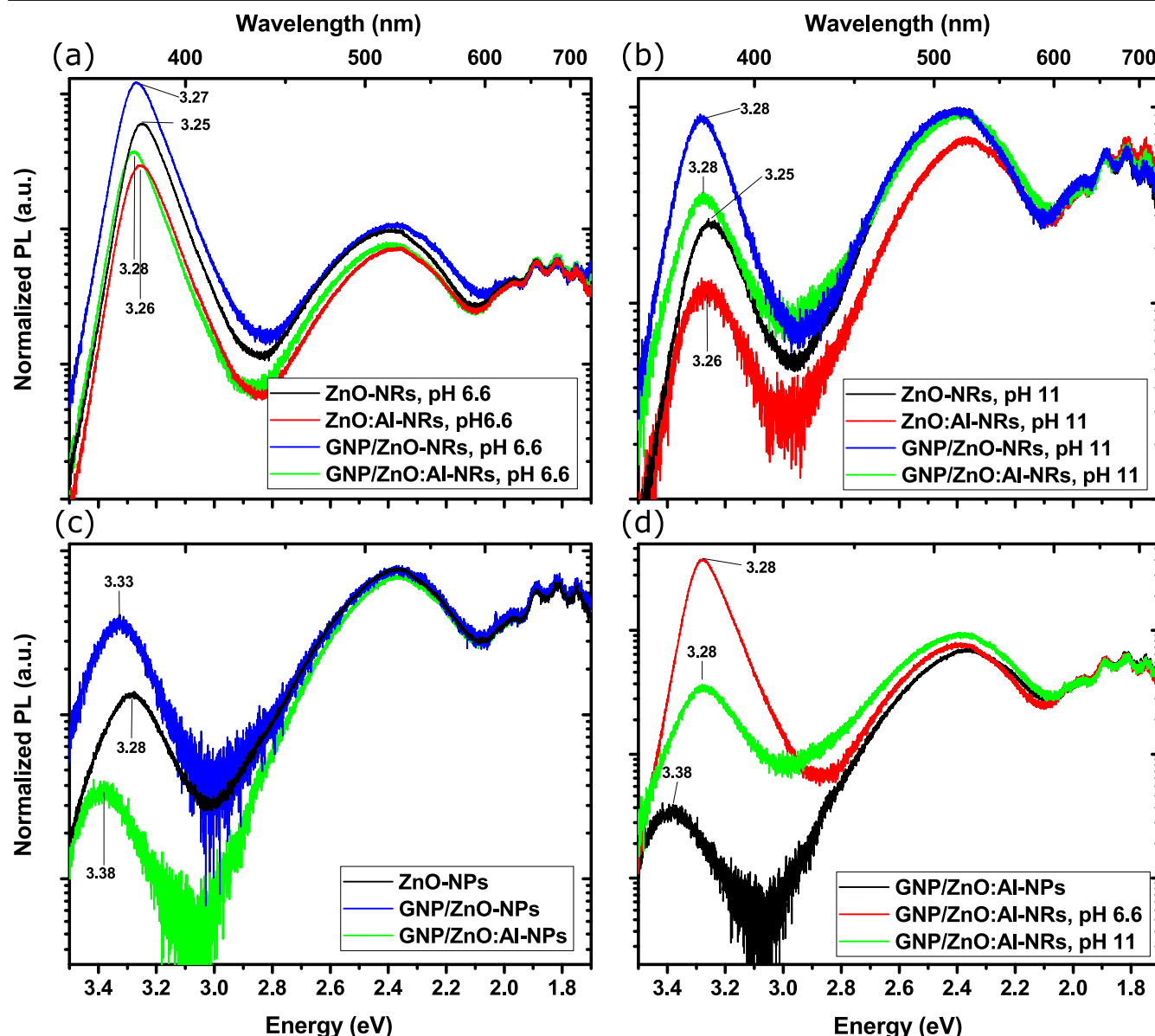


Figure 4. μ -PL room-temperature measurement for different ZnO-NRs composites grown at (a) pH 6.6, (b) pH 11, and (c) different GNP/ZnO-NPs composites. (d) Comparing PL spectra for GNP/ZnO:Al composites for three different ZnO morphologies.

the ZnO-NRs, room-temperature micro-PL (μ -PL) measurements were pursued on nanostructure deposits on gold coated silicon wafers using a 80 μ W, 266 nm laser excitation. The main peak in figure 4 shows the ZnO near-bandedge emission (NBE) at 3.25–3.38 eV in agreement with the absorption measurements. The broad peak at 2.4 eV indicates the visible light emission via deep levels in ZnO caused by zinc and oxygen vacancies [19]. The origin of the oscillations at 1.7–2 eV are not well understood but they are a common feature for all the samples. For easier comparison, all the PL data were normalized to the peak at 1.9 eV. Three sets of ZnO-nanorod morphologies (ZnO-NPs and ZnO-NRs grown at pH 6.6 and 11) in four different composites (undoped ZnO, ZnO:Al, GNP/ZnO, GNP/ZnO:Al) were investigated under the same conditions (figures 4(a)–(c)).

Two distinct changes are readily observed in the μ -PL spectra after doping the ZnO-NRs with Al; first, the deep level

emission (DLE) is suppressed due to filling of the defects levels by electrons (Al is a donor in ZnO). This observation has previously been reported for Ga-doped ZnO-NRs [26]. Furthermore, the NBE is also suppressed by Al-doping more significantly. The ratio of NBE-to-DLE integrated intensities ($I_{\text{NBE}}/I_{\text{DLE}}$) for different samples are summarized in table 1. In all the samples the $I_{\text{NBE}}/I_{\text{DLE}}$ ratio is decreased by adding Al to the composite. This decrease in the UV-to-visible emission ratio can be explained by introducing impurity levels in the bandgap with the doped metal ions and reducing the crystalline quality of ZnO [27–29]. Although it has been reported that post thermal treatment can improve the ZnO:Al crystallinity [28], our samples were measured without thermal treatment. Second, a blue-shift in the band-edge emission is observed which we attribute to the Burstein–Moss effect [23, 27, 30].

Another interesting general observation in the μ -PL spectra is that ZnO-NRs grown on GNPs exhibit a significantly stronger

Table 1. The NBE-to-DLE integrated intensity ratio ($I_{\text{NBE}}/I_{\text{DLE}}$) for different ZnO-NRs composites.

	Grown at pH 6.6	Grown at pH 11
ZnO-NRs	2.46	0.15
ZnO:Al-NRs	1.78	0.11
GNP/ZnO-NRs	4.25	0.46
GNP/ZnO:Al-NRs	1.85	0.21

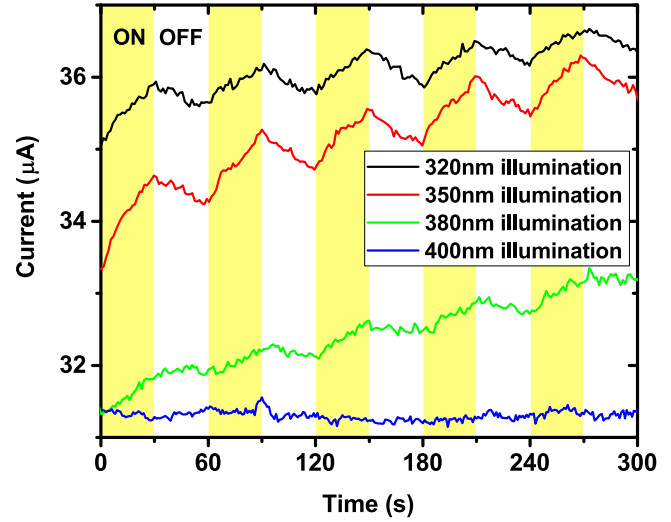
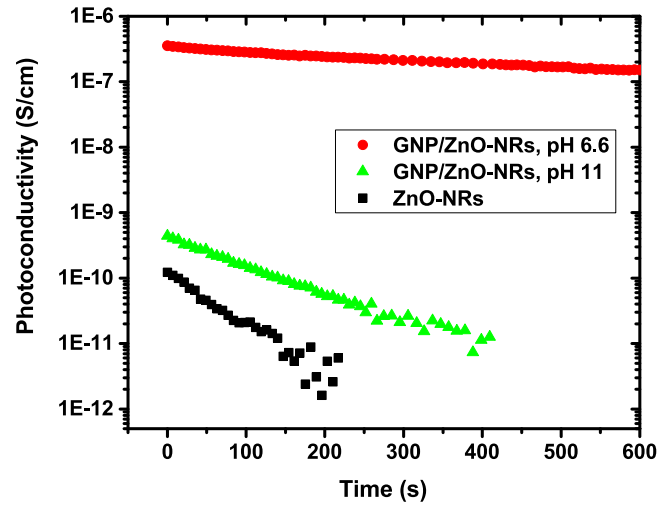
band-edge PL emission intensity compared to isolated ZnO-NRs. Previous reports in the literature attribute this to a reduction in the concentration of oxygen vacancy surface defects in the ZnO by oxygen groups adsorbed on the GNPs [31, 32] or more probably to resonant excitation of graphene plasmons [33–35].

Comparing the μ -PL for the two ZnO-NRs morphologies in figure 4(d) shows that thicker ZnO-NRs grown at pH 6.6 display a stronger band-edge PL emission than the thinner needle-like ZnO-NRs grown at pH 11 due to a lower surface-to-volume ratio. A high surface defect concentration on the thinner Zn-NRs not only causes a lower band-edge emission in the optical characteristics, but also leads to a higher electrical contact resistance (figure 2(b)).

To further support our conclusions, we measured the spectrally resolved photoconductivity of our samples. A significant persistent photoconductivity (PPC) in ZnO has been demonstrated in many articles [36–39]. The PPC observed in ZnO is attributed to a spatial charge separation mechanism induced by the built-in electric field caused by a surface space-charge layer [40]. Oxygen vacancies in the ZnO structure can chemically absorb oxygen from the air and become a hole trap. During illumination with photons with larger energy than the bandgap of ZnO, photogenerated holes will migrate to these surface traps and photodesorb the oxygen. At this point the separated mobile photoelectrons remain in the ZnO conduction band and result in a PPC.

Figure 5 below shows the results of pulsed optical excitation of an undoped GNP/ZnO-NR sample at 300 K. The measured current is recorded at a bias of 1 V under optical excitation with different wavelengths from 320 to 400 nm. There was no detected photoresponse for wavelengths longer than the corresponding bandgap energy. A large PPC effect was observed that increased at shorter wavelengths. In contrast, no PPC was observed in any of the highly Al-doped samples, not even under 254 nm illumination. This absence of PPC in highly doped samples can be explained by electrostatic screening of the surface oxygen ions that prevents holes from migrating towards the surface [40].

Time-resolved PPC was measured in detail to compare the effect of nanocomposite morphology on the lifetime of the photogenerated electrons. Figure 6 shows the time-dependence PPC of undoped GNP/ZnO-NR samples with different morphology after 350 nm excitation. After switching on the light, the surface chemisorbed oxygen traps the migrating photogenerated holes leaving behind an increasing density of mobile electrons in the conduction band, which results in an increasing PPC. Eventually, the complex processes involving

**Figure 5.** The cycled PPC response for a GNP/ZnO-NRs sample at 300 K and 1 V applied bias.**Figure 6.** Time-dependence of the PPC (σ_{ph}) after switching off the light for three different GNP/ZnO-NRs morphologies under 350 nm illumination at 300 K and 1 V applied bias.

charge carrier dynamics and surface oxygen chemisorption/desorption are in balance and the PPC saturates. By switching off the incident light, the PPC slowly decays due to recombination of photogenerated electrons and surface oxygen chemisorption. A detailed analysis of the continuity equation for the investigated complex composite materials is beyond the scope of this paper. Instead we focus on a more qualitative analysis of the decay process.

During the decay, the PPC is proportional to the density of electrons in the conduction band which in general decays stretched exponentially with time [41]. Evidently (figure 6), the photoconductivity (after subtracting the dark conductivity) σ_{ph} decays exponentially according to:

$$\frac{d\sigma_{ph}}{dt} = -\frac{\sigma_{ph}}{\tau_d}, \quad (1)$$

$$\ln \sigma_{ph} = -\frac{t}{\tau_d} + \ln \sigma_0. \quad (2)$$

Table 2. Dark conductivity (σ_d), PPC directly after switching off the light (σ_0) and excess electron lifetime (τ_d) of three different undoped samples at 300 K.

Sample	σ_d (S cm ⁻¹)	σ_0 (S cm ⁻¹)	τ_d (s)
ZnO-NRs	1.7×10^{-9}	1.1×10^{-10}	56
GNP/ZnO-NRs, pH 11	7.3×10^{-10}	3.9×10^{-10}	107
GNP/ZnO-NRs, pH 6.6	2.1×10^{-6}	3×10^{-7}	877

Here, τ_d is the decay time constant (excess electron lifetime) and σ_0 is the observed PPC directly after switching off the light. The extracted electron lifetime for samples with different morphology are calculated by a linear fitting to equation (2) and reported in table 2.

While the ZnO-NRs sample exhibits a long electron lifetime of about 56 s, the composite samples of graphene and ZnO-NRs have much longer electron lifetimes (107 and 877 s). The prolonged electron lifetime in these composites can be explained by an efficient transfer of photogenerated electrons to the graphene. This electron injection into the graphene causes a strongly reduced recombination rate and thus an enhanced PPC. The sample grown at pH 6.6 shows a significantly longer electron lifetime compared to the sample grown at pH 11. We conclude that the charge transfer between the ZnO-NRs and the graphene is more effective in the samples with thicker NRs grown at lower pH compared to the thinner needle-like NRs grown at higher pH.

The two morphologies of GNP/ZnO-NRs have different advantages and drawbacks. Thinner ZnO-NRs grown in a high pH solution exhibit a better dispersity and an improved attachment between the GNPs and ZnO-NRs, but also show a higher resistivity due to more surface defects and lower charge transfer between ZnO-NRs and GNPs. In contrast, the thicker ZnO-NRs grown at a lower pH display a lower resistivity and better charge transfer between ZnO-NRs and GNPs, but also a weaker GNP/ZnO-NRs bonding and a poorer dispersity. For conductive printing applications, lower resistance samples with thick ZnO-NRs are preferred. However, if the surface of the nanorod defects could be passivated by a proper post-growth treatment, the thinner GNP/ZnO-NRs morphology could be advantageous.

Growth and *in situ* doping of conjugated GNP/ZnO-NRs nanocomposites by a simple solution-based method as demonstrated in this work is economically desirable for mass production. For conductive purposes, the nanocomposite materials can be mixed by different polymers and tested for printing performance. Although we have primarily focused on conductive applications, our reported nanocomposites can be used in any optoelectronic, photochemical or photovoltaic application that requires high-porosity conjugated organic/semiconductor hybrids with a tunable conductance level.

4. Conclusion

In conclusion, we report on hydrothermal solution growth and characterization of different GNP/ZnO-NRs nanocomposites.

The ZnO-NRs were degenerately doped by Al for enhanced conductivity suitable for 3D-printing applications. Two different morphologies of ZnO-NRs, grown at different pH, were compared with respect to dispersity, GNP/ZnO-NRs bonding quality and conductivity. Our results show that a better graphene dispersion and improved bonding quality between the GNPs and NRs can be achieved in growth solutions with higher pH, however with a lower electrical conductivity in deposited GNP/ZnO-NRs layers. From μ -PL measurements we also infer that surface defects play an increasingly important role for thin ZnO-NRs with large surface-to-volume ratio. Although ZnO-NRs spacers on the GNPs surface decreases the conductivity between individual GNPs, they provide open free space porosities which promotes its capability to form a composite with other materials like thermoplastics and can be used in conductive bulk printing application, specifically 3D-printing. Finally, we demonstrate a strong enhancement in the PPC in undoped ZnO-NRs grown on graphene, compared to bare ZnO-NRs, which we attribute to an effective transfer of photogenerated electrons from the rods to the graphene.

Acknowledgments

The authors acknowledge financial support from the Knowledge Foundation, Linköping University and Halmstad University. The authors also thank Emil Nilsson and Urban Bilstrup for fruitful discussions.

ORCID iDs

Ebrahim Chalangar  <https://orcid.org/0000-0002-6850-1552>

Omer Nur  <https://orcid.org/0000-0002-9566-041X>

References

- [1] Jakus A E, Secor E B, Rutz A L, Jordan S W, Hersam M C and Shah R N 2015 Three-dimensional printing of high-content graphene scaffolds for electronic and biomedical applications *ACS Nano* **9** 4636–48
- [2] Leigh S J, Bradley R J, Purcell C P, Billson D R and D A Hutchins 2012 A simple, low-cost conductive composite material for 3D printing of electronic sensors *PLoS One* **7** e49365
- [3] Kamyshny A and Magdassi S 2014 Conductive nanomaterials for printed electronics *Small* **10** 3515–35
- [4] Bauhofer W and Kovacs J Z 2009 A review and analysis of electrical percolation in carbon nanotube polymer composites *Compos. Sci. Technol.* **69** 1486–98
- [5] Kim J H, Lee S, Wahat M, Jeong H, Chang W S, Jeong H J, Yang J-R, Kim J T and Seol S K 2016 Three-dimensional printing of highly conductive carbon nanotube microarchitectures with fluid ink *ACS Nano* **10** 8879–87
- [6] Ramasubramaniam R 2003 Homogeneous carbon nanotube/polymer composites for electrical applications *Appl. Phys. Lett.* **83** 2928–30

- [7] Weiss N O, Zhou H, Liao L, Liu Y, Jiang S, Huang Y and Duan X 2012 Graphene: an emerging electronic material *Adv. Mater.* **24** 5782–825
- [8] Li D, Muller M B, Gilje S, Kaner R B and Wallace G G 2008 Processable aqueous dispersions of graphene nanosheets *Nat. Nanotechnol.* **3** 101–5
- [9] Arapov K, Rubingh E, Abbel R, Laven J, de With G and Friedrich H 2016 Conductive screen printing inks by gelation of graphene dispersions *Adv. Funct. Mater.* **26** 586–93
- [10] Gao N and Fang X 2015 Synthesis and development of graphene inorganic semiconductor nanocomposites *Chem. Rev.* **115** 8294–343
- [11] Klingshirn C, Fallert J, Zhou H, Sartor J, Thiele C, Maier-Flaig F, Schneider D and Kalt H 2010 65 years of ZnO research old and very recent results *Phys. Status Solidi b* **247** 1424–47
- [12] Willander M *et al* 2009 Zinc oxide nanorod based photonic devices: recent progress in growth, light emitting diodes and lasers *Nanotechnology* **20** 332001
- [13] Amin G, Asif M H, Zainelabdin A, Zaman S, Nur O and Willander M 2011 Influence of pH, precursor concentration, growth time, and temperature on the morphology of ZnO nanostructures grown by the hydrothermal method *J. Nanomater.* **2011** 5:5
- [14] Munshi A M, Dheeraj D L, Fauske V T, Kim D-C, van Helvoort A T J, Fimland B-O and Weman H 2012 Vertically aligned GaAs nanowires on graphite and few-layer graphene: generic model and epitaxial growth *Nano Lett.* **12** 4570–6
- [15] Larson K, Clark A, Appel A, Dai Q, He H and Zygmunt S 2015 Surface-dependence of interfacial binding strength between zinc oxide and graphene *RSC Adv.* **5** 65719–24
- [16] Choi W M, Shin K-S, Lee H S, Choi D, Kim K, Shin H-J, Yoon S-M, Choi J-Y and Kim S-W 2011 Selective growth of ZnO nanorods on SiO₂/Si substrates using a graphene buffer layer *Nano Res.* **4** 440–7
- [17] Lin J, Penchev M, Wang G, Paul R K, Zhong J, Jing X, Ozkan M and Ozkan C S 2010 Heterogeneous graphene nanostructures: ZnO nanostructures grown on large-area graphene layers *Small* **6** 2448–52
- [18] Hwang J O, Lee D H, Kim J Y, Han T H, Kim B H, Park M, No K and Kim S O 2011 Vertical ZnO nanowires/graphene hybrids for transparent and flexible field emission *J. Mater. Chem.* **21** 3432–7
- [19] Alnoor H, Pozina G, Khranovskyy V, Liu X, Iandolo D, Willander M and Nur O 2016 Influence of ZnO seed layer precursor molar ratio on the density of interface defects in low temperature aqueous chemically synthesized ZnO nanorods/GaN light-emitting diodes *J. Appl. Phys.* **119** 165702
- [20] Brsan O A, Hoffmann G G, van der Ven L G J and de With G 2016 Single-walled carbon nanotube networks: the influence of individual tube–tube contacts on the large-scale conductivity of polymer composites *Adv. Funct. Mater.* **26** 4377–85
- [21] Fuchs P, Hagendorfer H, Romanyuk Y E and Tiwari A N 2015 Doping strategies for highly conductive Al-doped ZnO films grown from aqueous solution *Phys. Status Solidi a* **212** 51–5
- [22] Miyake M, Fukui H and Hirato T 2012 Preparation of Al-doped ZnO films by aqueous solution process using a continuous circulation reactor *Phys. Status Solidi a* **209** 945–8
- [23] Edinger S, Bansal N, Bauch M, Wibowo R A, Hamid R, Trimmel G and Dimopoulos T 2017 Comparison of chemical bath-deposited ZnO films doped with Al, Ga and In *J. Mater. Sci.* **52** 9410–23
- [24] Chandraiahgari C R, De Bellis G, Balijepalli S K, Kaciulis S, Ballirano P, Migliori A, Morandi V, Caneve L, Sarto F and Sarto M S 2016 Control of the size and density of ZnO-nanorods grown onto graphene nanoplatelets in aqueous suspensions *RSC Adv.* **6** 83217–25
- [25] Podbrek P, Draí G, Paramo J A, Strzemechny Y M, Maek J and Orel Z C 2010 Growth of zinc oxide particles in the presence of silicon *CrystEngComm* **12** 3071–9
- [26] Sakurai M, Wang Y G, Uemura T and Aono M 2009 Electrical properties of individual ZnO nanowires *Nanotechnology* **20** 155203
- [27] Zhu Q, Xie C, Li H, Yang C, Zhang S and Zeng D 2014 Selectively enhanced UV and NIR photoluminescence from a degenerate ZnO nanorod array film *J. Mater. Chem. C* **2** 4566–80
- [28] Wang M, Lee K E, Hahn S H, Kim E J, Kim S, Chung J S, Shin E W and Park C 2007 Optical and photoluminescent properties of sol-gel Al-doped ZnO thin films *Mater. Lett.* **61** 1118–21
- [29] Rahman M M, Khan M K R, Rafiqul Islam M, Halim M A, Shahjahan M, Hakim M A, Saha D K and Khan J U 2012 Effect of Al doping on structural, electrical, optical and photoluminescence properties of nano-structural ZnO thin films *J. Mater. Sci. Technol.* **28** 329–35
- [30] Ziabari A A and Rozati S M 2012 Carrier transport and bandgap shift in n-type degenerate ZnO thin films: the effect of band edge nonparabolicity *Physica B* **407** 4512–7
- [31] Lee E, Kim J-Y, Kwon B J, Jang E-S and An S J 2014 Vacancy filling effect of graphene on photoluminescence behavior of ZnO/graphene nanocomposite *Phys. Status Solidi* **8** 836–40
- [32] Pham C V, Repp S, Thomann R, Krueger M, Weber S and Erdem E 2016 Charge transfer and surface defect healing within ZnO nanoparticle decorated graphene hybrid materials *Nanoscale* **8** 9682–7
- [33] Hwang S W *et al* 2010 Plasmon-enhanced ultraviolet photoluminescence from hybrid structures of graphene/ZnO films *Phys. Rev. Lett.* **105** 127403
- [34] Zhang S G, Wen L, Li J L, Gao F L, Zhang X W, Li L H and Li G Q 2014 Plasmon-enhanced ultraviolet photoluminescence from highly ordered ZnO nanorods/graphene hybrid structure decorated with Au nanospheres *J. Phys. D: Appl. Phys.* **47** 495103
- [35] Liu R, Fu X-W, Meng J, Bie Y-Q, Yu D-P and Liao Z-M 2013 Graphene plasmon enhanced photoluminescence in ZnO microwires *Nanoscale* **5** 5294–8
- [36] Medved D B 1961 Photoconductivity and chemisorption kinetics in sintered zinc oxide semiconductor *J. Phys. Chem. Solids* **20** 255–67
- [37] Chen M-W, Chen C-Y, Lien D-H, Ding Y and He J-H 2010 Photoconductive enhancement of single ZnO nanowire through localized Schottky effects *Opt. Express* **18** 14836–41
- [38] Moore J C and C V Thompson 2013 A phenomenological model for the photocurrent transient relaxation observed in ZnO-based photodetector devices *Sensors* **13** 9921–40
- [39] Zhu Q, Xie C, Li H, Zhang J and Zeng D 2015 Through-process analytical modeling of photoconductance spectrum for porous ZnO nanocrystalline film *Chem. Mater.* **27** 2861–74
- [40] Zhu Q, Xie C, Li H and Zeng D 2016 A method for modeling and deciphering the persistent photoconductance and long-term charge storage of ZnO nanorod arrays *Nano Res.* **9** 2972–3002
- [41] Rani M and Tripathi S K 2016 Electron transfer properties of organic dye sensitized ZnO and ZnO/TiO₂ photoanode for dye sensitized solar cells *Renew. Sustain. Energy Rev.* **61** 97–107